Computers and Concrete, *Vol. 25, No. 2* (*2020*) *181-192*
DOI: https://doi.org/10.12989/cac.2020.25.2.181

FEM investigation of SFRCs using a substepping integration of constitutive equations

Gholamreza B. Golpasand[a], Masood Farzam* and Siamak S. Shishvan[b]

Department of Structural Engineering, University of Tabriz, Tabriz, Iran

(*Received August 21, 2019, Revised February 6, 2020, Accepted February 12, 2020*)

Abstract. Nowadays, steel fiber reinforced concretes (SFRCs) are widely used in practical applications. Significant experimental research has thus been carried out to determine the constitutive equations that represent the behavior of SFRCs under multiaxial loadings. However, numerical modelling of SFRCs via FEM has been challenging due to the complexities of the implementation of these constitutive equations. In this study, following the literature, a plasticity model is constructed for the behavior of SFRCs that involves the Willam-Warnke failure surface with the relevant evolution laws and a non-associated flow rule for determining the plastic deformations. For the precise (yet rapid) integration of the constitutive equations, an explicit substepping scheme consisting of yield intersection and drift correction algorithms is employed and thus implemented in ABAQUS via UMAT. The FEM model includes various material parameters that are determined from the experimental data. Three sets of parameters are used in the numerical simulations. While the first set is from the experiments that are conducted in this study on SFRC specimens with various contents of steel fibers, the other two sets are from the experiments reported in the literature. The response of SFRCs under multiaxial compression obtained from various numerical simulations are compared with the experimental data. The good agreement between numerical results and the experimental data indicates that not only the adopted plasticity model represents the behavior of SFRCs very well but also the implemented integration scheme can be employed in practical applications of SFRCs.

Keywords: steel fiber reinforced concrete (SFRC); finite element method (FEM); concrete constitutive models; non-linear analysis; software development and applications

1. Introduction

Recent advances in concrete technology have led to the production of various types of fiber reinforced concrete (FRC) which have been widely used in many application as the fibers can improve the behavior of plain concrete in many aspects. Increasing the tensile strength and improving brittle behavior (Balaguru and Shah 1992, Gul *et al.* 2014) with preventing sudden failure are the main advantages of using FRCs in a wide range of structures, specifically in complex geometry structures. Various types of fibers such as steel microfiber, long hooked steel fiber, polypropylene fiber and mixed form of them were considered in the literature (Chun and Yoo 2019, Han *et al.* 2019, Lee *et al.* 2019, Pantazopoulou and Zanganeh 2001, Poorhoseina and Nematzadeh 2018, Zhang *et al.* 2018). Extensive studies on the mechanical properties of FRCs have shown that the presence of fibers not only increases the tensile strength (Amin *et al.* 2017, Zhang *et al.* 2018), but also stabilizes the cracks in the concrete (Amin *et al.* 2017, Balaguru and Shah 1992, Barros *et al.* 2011, Perumal 2014). It should however be noted that the experimental studies showed that the fibers have minor effects on the compressive strength of concrete (Balaguru and Shah 1992).

In recent years, many experimental studies have been conducted to examine the behavior of FRCs under multiaxial stresses and to propose appropriate constitutive equations for FRCs (Ansari and Li 1998, Lu and Hsu 2006, Ren *et al.* 2018). For example, Pantazopoulou and Zanganeh (2001) have experimentally investigated the triaxial behavior of FRCs where the structural properties of FRCs were defined based on the type and amount of fibers, load path, test conditions and specimen size. Moreover, the effect of confinement on ductility and plastic behavior of FRCs was experimentally investigated by Farnam *et al.* (2010). Recently, Jiang *et al.* (2017) performed experiments on FRCs under different loading patterns considering passive confinements.

On the other hand, constitutive equations used in numerical modelling of concrete behavior under multiaxial stresses received significant attention due to intrinsic complexities of conducting multiaxial compression tests on concrete (Chen 2007). Various theories including plasticity models (Chi *et al.* 2013, Grassl *et al.* 2002, Imran and Pantazopoulou 2001), concrete damage plasticity (CDP) model (Othman and Marzouk 2018) and microplane models (Bažant *et al.* 2000, Smolčić and Ožbolt 2017) have been introduced to represent concrete behavior. Such theories can

*Corresponding author, Assistant Professor
E-mail: mafarzam@tabrizu.ac.ir
[a]Ph.D. Student
E-mail: g.golpasand@tabrizu.ac.ir
[b]Associate Professor
E-mail: sshishvan@tabrizu.ac.ir

http://www.techno-press.org/?journal=cac&subpage=8
ISSN: 1598-8198 (Print), 1598-818X (Online)

in principle be employed to study the behavior of FRCs. Indeed, some of these models are incorporated in commercial finite element analysis (FEA) packages that enables researchers to use them in studying the mechanical behavior of FRCs. However, there exist constitutive models, such as the Willam-Warnke (W-W) five-parameter model for concrete plasticity (William and Warnke 1975), that can represent concrete behavior very well but have not been included in commercial FEA softwares yet. This model has been successfully employed by Yin-Chi *et al.* (Chi *et al.* 2013, 2014) to study the behavior of hybrid fiber reinforced concretes (HFRC) under multiaxial compression. Moreover, Ana Blanco *et al.* (2014) proposed new constitutive equations based on the Barcelona experiment and compared their numerical results with the associated experimental data. Recently, a model was presented for numerical analysis of FRCs where the concrete and fibers were separately modelled (Liang and Wu 2018).

The constitutive models for plain concrete and FRCs are typically complex and require significant efforts for their implementation in the numerical FEA models. Specifically, they require a precise (yet rapid) integration scheme. Various explicit/implicit integration schemes with their own pros and cons were proposed in the literature (Bitencourt *et al.* 2019). Typically, an explicit integration scheme is preferred for complex constitutive models to avoid higher-order derivatives (Rodrigues *et al.* 2018).

In the present study, a plasticity model is adopted to numerically investigate the behavior of steel fiber reinforced concrete (SFRC) under multiaxial compression. This model involves the W-W constitutive model for the plastic behavior of SFRC as introduced in (William and Warnke 1975) and (Chi *et al.* 2014) and the non-associated flow rule of Grassl *et al.* (2002) for determining the plastic deformations. Following (Chi *et al.* 2012, Guo 1997, Lan and Guo 1997), the pre-peak and post-peak behavior in the response of SFRC is included in the model via a hardening/softening function. The model includes various material parameters that are determined from the experimental data. Three sets of parameters are given. The first set is from the experiments that we conduct in this study on SFRC specimens with various contents of steel fibers. The other two sets of parameters are from the experiments that Pantazopoulou and Zanganeh (2001) and Chern *et al.* (1993) conducted on SFRCs. For the integration of the constitutive equations, we use the modified explicit substepping algorithm of Sloan *et al.* (2001) which is based on the algorithm of Sloan (1987) with some critical enhancements such as yield intersection and drift correction algorithms. This integration scheme which is presented in details in section 3 is implemented in ABAQUS (Hibbit *et al.* 2005) via UMAT. Various numerical simulations are carried out on SFRCs under multiaxial compression and the obtained stress-strain curves are then compared with the experimental data. The numerical results are found in a good agreement with the experimental data indicating that not only the adopted plasticity model represents the response of SFRCs very well, in line with the literature (Chern *et al.* 1993, Pantazopoulou and Zanganeh 2001), but also the implemented integration scheme can be employed in practical applications of SFRCs in complex geometry structures.

2. The constitutive equations

The constitutive equations for SFRCs are determined based on the plasticity model adopted here and involve the failure surface, the evolution of the loading surface (i.e., hardening/softening) and the flow rule as presented in the following.

2.1 Failure surface

For the analysis of FRC under multiaxial stresses, the W-W five-parameter failure criterion (William and Warnke, 1975) has been employed in the literature, e.g., (Chi *et al.* 2014, Swaddiwudhipong and Seow 2006). Using Haigh-Westergard coordinates, the W-W failure surface for SFRC is expressed via

$$F(\xi,\rho,\theta)=\rho-K(\bar{\varepsilon}_p)\rho^f(\xi,\theta)=0. \tag{1}$$

Here, $K(\bar{\varepsilon}_{\rm p})$ denotes the hardening/softening function, $\rho=\sqrt{2J_2}$ with $J_2=s_{ij}s_{ij}/2$ the second invariant of the deviatoric stress tensor s_{ij}, $\xi=I_1/\sqrt{3}$ with $I_1=\sigma_{kk}$ and θ is the Lode angle with $\cos\theta=\frac{2\sigma_1-\sigma_2-\sigma_3}{2\sqrt{3J_2}}$ for principal stresses $\sigma_1\geq\sigma_2\geq\sigma_3$. In this five-parameter model, $\rho^{\rm f}(\xi,\theta)$ describing the ellipsoidal shape of deviatoric length is given by (Chen and Han 2012, Chi *et al.* 2014)

$$\rho^{\rm f}(\xi,\theta)= \frac{2\rho_{\rm c}^{\rm f}\left[(\rho_{\rm c}^{\rm f})^2-(\rho_{\rm t}^{\rm f})^2\right]\cos\theta+\rho_{\rm c}^{\rm f}(2\rho_{\rm t}^{\rm f}-\rho_{\rm c}^{\rm f})}{4\left[(\rho_{\rm c}^{\rm f})^2-(\rho_{\rm t}^{\rm f})^2\right]\cos^2\theta+(\rho_{\rm c}^{\rm f}-2\rho_{\rm t}^{\rm f})^2} \frac{\left\{4\left[(\rho_{\rm c}^{\rm f})^2-(\rho_{\rm t}^{\rm f})^2\right]\cos^2\theta+5(\rho_{\rm t}^{\rm f})^2-4\rho_{\rm t}^{\rm f}\rho_{\rm c}^{\rm f}\right\}^{1/2}}{4\left[(\rho_{\rm c}^{\rm f})^2-(\rho_{\rm t}^{\rm f})^2\right]\cos^2\theta+(\rho_{\rm c}^{\rm f}-2\rho_{\rm t}^{\rm f})^2} \tag{2}$$

that is defined to interpolate between the tensile meridian $\rho_{\rm t}^{\rm f}$ (where $\theta=0$) and the compressive meridian $\rho_{\rm c}^{\rm f}$ (where $\theta=60°$) which are expressed via

$$\begin{aligned}\frac{\xi}{f_{\rm c}'}&=\hat{a}_0+\hat{a}_1\frac{\rho_{\rm t}^{\rm f}}{f_{\rm c}'}+\hat{a}_2\left(\frac{\rho_{\rm t}^{\rm f}}{f_{\rm c}'}\right)^2,\\ \frac{\xi}{f_{\rm c}'}&=\hat{b}_0+\hat{b}_1\frac{\rho_{\rm c}^{\rm f}}{f_{\rm c}'}+\hat{b}_2\left(\frac{\rho_{\rm c}^{\rm f}}{f_{\rm c}'}\right)^2.\end{aligned} \tag{3}$$

While $f_{\rm c}'$ is the compressive strength of the SFRC, the material constants $\hat{a}_0,\ldots,\hat{b}_2$ are typically determined using experimental data on SFRC (note that $\hat{a}_0=\hat{b}_0$ so as the tensile and compressive meridians intersect with the hydrostatic axis at equal tension). It is sometimes convenient to rewrite relations in Eq. (3) in the following forms

$$\begin{aligned}\frac{\tau_{\rm mt}}{f_{\rm c}'}&=a_0+a_1\frac{\sigma_{\rm m}}{f_{\rm c}'}+a_2\left(\frac{\sigma_{\rm m}}{f_{\rm c}'}\right)^2,\\ \frac{\tau_{\rm mc}}{f_{\rm c}'}&=b_0+b_1\frac{\sigma_{\rm m}}{f_{\rm c}'}+b_2\left(\frac{\sigma_{\rm m}}{f_{\rm c}'}\right)^2,\end{aligned} \tag{4}$$

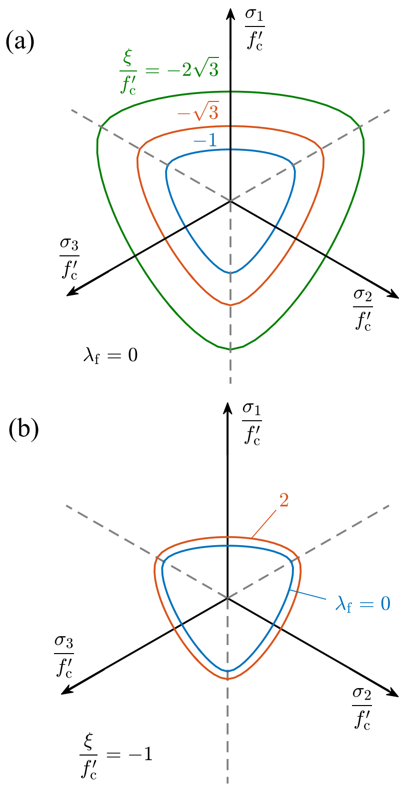

Fig. 1 Variation of yield loci with the change of (a) ξ/f_c' and (b) λ_f in the deviatoric plane for SFRC. For associated material parameters see section 4

where $\tau_{mt} \equiv \rho_t^f/\sqrt{5}$ and $\tau_{mc} \equiv \rho_c^f/\sqrt{5}$ represent mean shear stresses for $\theta = 0$ and $\theta = 60°$, respectively, and $\sigma_m \equiv \xi/\sqrt{3}$ is the mean normal stress.

Following (Chi *et al*. 2013, 2014, Swaddiwudhipong and Seow 2006), the effect of steel fibers is specifically included in the yield surface (1) via parameters k_t and k_c as follows

$$\begin{aligned} \rho_t^f &= k_t \rho_t, \\ \rho_c^f &= k_c \rho_c. \end{aligned} \tag{5}$$

with ρ_t the tensile meridian and ρ_c the compressive meridian of plain concrete. Parameters k_t and k_c are given as (Chi *et al*. 2013, 2014, Swaddiwudhipong and Seow 2006)

$$k_t = 1 + 0.08\lambda_f\,, \tag{6}$$

and

$$k_c = 1 + 0.056\lambda_f\,, \tag{7}$$

where the fiber reinforcement index of steel fibers is given by

$$\lambda_f = V_f \frac{l_f}{d_f}. \tag{8}$$

Here, V_f and l_f/d_f are the volume fraction and the aspect ratio of steel fibers, respectively. As indicated in (Chi *et al*. 2014), while with increasing k_t the yield locus in π-plane (deviatoric plane) is changed from a rounded triangular shape to a circular one, with increasing k_c the corners of the triangular shape become sharper (yet rounded).

Fig. 1(a) shows the yield loci for SFRC in the deviatoric plane as defined in Eq. (1) for various values of ξ/f_c' and $\lambda_f = 0$, i.e., plain concrete. As mentioned above, steel fibers affect the yield surface via the fiber reinforcement index λ_f through parameters k_t and k_c as given in Eqs. (6)-(7). Fig. 1(b) shows the variation of yield locus for $\xi/f_c' = -1$ with the change of λ_f in the range from 0 to 2 that is used in practical applications of SFRCs. We now proceed to introduce the hardening/softening function $K(\bar{\varepsilon}_p)$ which is used for the evolution of the yield surface.

2.2 Evolution of the loading surface

In Eq. (1), the hardening/softening function $K(\bar{\varepsilon}_p)$ represents the pre-peak and post-peak behavior in the response of SFRC. $K(\bar{\varepsilon}_p)$ has an initial value of K_{initial} in the absence of plastic deformations and is taken to be a function of equivalent plastic strain (Chi *et al*. 2012, Guo 1997) defined as $\bar{\varepsilon}_p = \int d\bar{\varepsilon}_p = \int \sqrt{\frac{2}{3} d\varepsilon_{ij}^p d\varepsilon_{ij}^p}$ where $d\varepsilon_{ij}^p$ are components of the plastic strain increment tensor. With this form of $K(\bar{\varepsilon}_p)$, the loading surface remains similar to the failure surface, i.e., evolution of the failure surface during deformations is assumed to be isotropic with $dK(\bar{\varepsilon}_p) = H_p\, d\bar{\varepsilon}_p$ where H_p is the hardening/softening modulus. Following Chi *et al*. (2012, 2014), the mathematical description of the hardening function is based on the ascending part of Guo parabola (Chi *et al*. 2012, Lan and Guo 1997) and, in a rate form, is written as

$$\begin{aligned} dK(\bar{\varepsilon}_p) = H_p\, d\bar{\varepsilon}_p \equiv \Bigg[& a\frac{1}{\varepsilon_c} + 2(3-2a)\frac{\bar{\varepsilon}}{\varepsilon_c}\frac{1}{\varepsilon_c} \\ & +3(a-2)\left(\frac{\bar{\varepsilon}}{\varepsilon_c}\right)^2 \frac{1}{\varepsilon_c}\Bigg] d\bar{\varepsilon}_p, \quad \bar{\varepsilon} \le \varepsilon_c \end{aligned} \tag{9}$$

Similarly, in the softening region, the rate form of the softening function is given by Chi *et al*. (2012, 2013)

$$\begin{aligned} & dK(\bar{\varepsilon}_p) = H_p\, d\bar{\varepsilon}_p \equiv \\ & \frac{\frac{1}{\varepsilon_c}\left[b\left(\frac{\bar{\varepsilon}}{\varepsilon_c}-1\right)^2 + \frac{\bar{\varepsilon}}{\varepsilon_c}\right] - \frac{\bar{\varepsilon}}{\varepsilon_c}\left[2b\left(\frac{\bar{\varepsilon}}{\varepsilon_c}-1\right)\frac{1}{\varepsilon_c} + \frac{1}{\varepsilon_c}\right]}{\left[b\left(\frac{\bar{\varepsilon}}{\varepsilon_c}-1\right)^2 + \frac{\bar{\varepsilon}}{\varepsilon_c}\right]^2} d\bar{\varepsilon}_p, \\ & \bar{\varepsilon} \ge \varepsilon_c \end{aligned} \tag{10}$$

which represents the descending part of stress-strain response (Lan and Guo 1997). Parameters a and b in above equations control the slope of the hardening/softening behavior, respectively, and are dependent on the fiber contents of SFRC. Following Chi *et al*. (2012, 2014), they are given as

$$\begin{aligned} a &= 28.2283 - 23.2771 f_c'^{\,0.0374} + 0.4772\lambda_f\,, \\ b &= 0.01 + 0.037 f_c'^{\,0.2846} - 0.02372\lambda_f \quad . \end{aligned} \tag{11}$$

where f_c' is in units of MPa. Moreover, in Eqs. (9)-(10), $\bar{\varepsilon}$ is the equivalent total strain defined as

$$\bar{\varepsilon} = \frac{1}{3}\sqrt{\left\{2\left[(\varepsilon_{xx}-\varepsilon_{yy})^2 + (\varepsilon_{yy}-\varepsilon_{zz})^2 + (\varepsilon_{xx}-\varepsilon_{zz})^2\right]\right.} \tag{12}$$

$$\sqrt{+3\left(\varepsilon_{xy}^2+\varepsilon_{yz}^2+\varepsilon_{xz}^2\right)\}}$$

and ε_{c} is the value of equivalent total strain at which a hardening response switches to a softening one. The value of ε_{c} was suggested to be taken as (Chi *et al*. 2014)

$$\varepsilon_{\mathrm{c}} = 263.3\times 10^{-6}\sqrt{f_{\mathrm{c}}'(1+0.206\lambda_{\mathrm{f}})}\left(1+8.5\frac{\sigma_1+\sigma_2}{f_{\mathrm{c}}'}\right), \quad (13)$$

where σ_1 and σ_2 represent the lateral (compressive) principal stresses with σ_3 being the major (compressive) principal stress.

2.3 Non-associated flow rule

For concrete material whose behavior depends on hydrostatic stress, the non-associated flow rule is typically used (e.g., Chen 2007, Chen and Han 2012, Chi *et al*. 2017) in the calculation of plastic deformations. Specifically, the plastic strain increment follows from

$$d\varepsilon_{ij}^{\mathrm{p}} = d\lambda\frac{\partial g}{\partial\sigma_{ij}}\ , \quad (14)$$

in terms of plastic multiplier $d\lambda$. Accordingly, the equivalent plastic strain is obtained via $d\bar{\varepsilon}_{\mathrm{p}} = d\lambda\sqrt{\frac{2}{3}\frac{\partial g}{\partial\sigma_{ij}}\frac{\partial g}{\partial\sigma_{ij}}} \equiv d\lambda\sqrt{\frac{2}{3}}\left\|\frac{\partial g}{\partial\boldsymbol{\sigma}}\right\|$. Here, $g\neq F$ is the plastic potential function which, in the Haigh-Westergard coordinates, is given as

$$g \equiv -A\bar{\rho}^2 - B\bar{\rho} + \bar{\xi} + C = 0\,, \quad (15)$$

where the model of Grassl *et al*. (2002) for plain concrete was adopted with $\bar{\xi} = \xi/f_{\mathrm{c}}'$ and $\bar{\rho} = \rho/f_{\mathrm{c}}' \equiv \sqrt{2J_2}/f_{\mathrm{c}}'$. Following Chi *et al*. (2012, 2014), the inclination defined based on this plastic potential is thus given as $\phi \equiv -d\bar{\xi}/d\bar{\rho} = -2A\bar{\rho} - B$. The two parameters A and B are obtained according to the axial strain in the compressive strength test at the peak stress (where $\phi_1 = -2A\bar{\rho}_1 - B$) as well as the axial strain in the triaxial pressure test at the maximum stress (where $\phi_2 = -2A\bar{\rho}_2 - B$); see (Grassl *et al*. 2002) for more details. Solving these two equations, we obtain

$$A = \frac{\phi_2-\phi_1}{2(\bar{\rho}_1-\bar{\rho}_2)}$$
$$B = \rho_1\frac{\phi_1-\phi_2}{\bar{\rho}_1-\bar{\rho}_2} - \phi_1 \quad (16)$$

2.4 Stress-strain relations

The relation between the stress and the elastic strain increments can be established by means of Hooke's law, i.e.

$$d\sigma_{ij} = C_{ijkl}^{\mathrm{e}}d\varepsilon_{kl}^{\mathrm{e}} = C_{ijkl}^{\mathrm{e}}\left(d\varepsilon_{kl} - d\varepsilon_{kl}^{\mathrm{p}}\right), \quad (17)$$

where additive decomposition of elastic and plastic strain increments are considered. For isotropic materials, the elasticity tensor C_{ijkl}^{e} is expressed as

$$C_{ijkl}^{\mathrm{e}} = 2G\left(\delta_{ik}\delta_{jl} + \frac{\nu}{1-2\nu}\delta_{ij}\delta_{kl}\right), \quad (18)$$

with G the shear modulus, ν the Poisson's ratio and δ_{ij} the Kronecker delta function. The plastic strain increment $d\varepsilon_{kl}^{\mathrm{p}}$ is determined from the non-associated flow rule (14) wherein the plastic multiplier $d\lambda$ is determined using the consistency condition, i.e., $dF = 0$ with F given in Eq. (1), as follows

$$d\lambda = \frac{\frac{\partial F}{\partial\sigma_{ij}}C_{ijkl}^{\mathrm{e}}\,d\varepsilon_{kl}}{\frac{\partial F}{\partial\sigma_{mn}}C_{mnpq}^{\mathrm{e}}\frac{\partial g}{\partial\sigma_{pq}} - \frac{\partial F}{\partial K}H_{\mathrm{p}}\sqrt{\frac{2}{3}}\left\|\frac{\partial g}{\partial\boldsymbol{\sigma}}\right\|}, \quad (19)$$

Note that H_{p} is the hardening/softening modulus that is given in Eqs. (9)-(10). By substituting Eqs. (14)-(19) into Eq. (17) and solving for $d\sigma_{ij}$, we obtain

$$d\sigma_{ij} = C_{ijkl}^{\mathrm{ep}}d\varepsilon_{kl} \equiv \left(C_{ijkl}^{\mathrm{e}} - \frac{C_{ijmn}^{\mathrm{e}}\frac{\partial g}{\partial\sigma_{mn}}\left(\frac{\partial F}{\partial\sigma_{pq}}\right)^T C_{pqkl}^{\mathrm{e}}}{\frac{\partial F}{\partial\sigma_{rs}}C_{rstu}^{\mathrm{e}}\frac{\partial g}{\partial\sigma_{tu}} - \frac{\partial F}{\partial K}H_{\mathrm{p}}\sqrt{\frac{2}{3}}\left\|\frac{\partial g}{\partial\boldsymbol{\sigma}}\right\|}\right)d\varepsilon_{kl}\,, \quad (20)$$

where C_{ijkl}^{ep} denotes the elasto-plastic stiffness tensor. This relation completes the constitutive equations and we now proceed to explain the numerical integration of these equations.

3. Integration of constitutive equations

During a typical increment or iteration of a nonlinear finite element analysis, the forces are incrementally applied and the solution of the global stiffness equations results in the corresponding nodal displacement increments. Once these displacements are known, the strain increments at the integration points within each element are determined using the strain-displacement relations. Determining stresses associated with an imposed strain increment at an integration point is typically referred to as integration of constitutive equations.

For the integration of constitutive equations of SFRCs, described in Section 2, Chi *et al*. (2014) used the algorithm of Sloan (1987). Here, we use the modified explicit substepping algorithm of Sloan *et al*. (2001) which is based on the algorithm of Sloan (1987) with some critical enhancements such as yield intersection and drift correction algorithms. At an integration point, the strain in the beginning of increment is used to calculate the hardening/softening modulus H_{p} and this value is kept unchanged during the substepping algorithm. The strain increment $\Delta\boldsymbol{\varepsilon}$ is divided into N^s substeps, i.e., $\Delta\boldsymbol{\varepsilon}^{\mathrm{s}} = \Delta\boldsymbol{\varepsilon}/N^s$ and three main tasks are done for each substep: (i) finding the intersection with yield surface using Pegasus method (Dowell and Jarratt 1972), (ii) calculating the values of stress and hardening/softening parameter according to the algorithm of Sloan *et al*. (2001), and (iii) resorting the stresses to the yield surface via drift control (Sloan *et al*. 2001). Specifically, assuming that the stress and hardening parameter at the beginning of the substep are denoted by $\boldsymbol{\sigma}_0$ and K_0, respectively, while they are denoted by $\boldsymbol{\sigma}_1$ and K_1 at the end of the substep, following calculations are carried out for each substep:

1. If $F(\boldsymbol{\sigma}_0 + \boldsymbol{C}^{\mathrm{e}}:\Delta\boldsymbol{\varepsilon}^{\mathrm{s}}, K_0) < FTOL$, then $\boldsymbol{\sigma}_{\mathrm{b}} = \boldsymbol{\sigma}_0 + \boldsymbol{C}^{\mathrm{e}}:\Delta\boldsymbol{\varepsilon}^{\mathrm{s}}$ and $K_{\mathrm{b}} = K_0$; go to item 5.

2. Find the intersection with the yield surface, i.e. the value of α, as follows:

2.1 Set $\alpha_{\mathrm{c}} = 0$ and $\alpha_{\mathrm{d}} = 1$.

2.2 Set $F_{\mathrm{c}} = F(\boldsymbol{\sigma}_0 + \alpha_{\mathrm{c}}\boldsymbol{C}^{\mathrm{e}}:\Delta\boldsymbol{\varepsilon}^{\mathrm{s}}, K_0)$, $F_{\mathrm{d}} = F(\boldsymbol{\sigma}_0 + \alpha_{\mathrm{d}}\boldsymbol{C}^{\mathrm{e}}:\Delta\boldsymbol{\varepsilon}^{\mathrm{s}}, K_0)$ and $F_{\mathrm{n}} = F_{\mathrm{d}}$.

2.3 Do While $F_{\mathrm{n}} > FTOL$

2.3.1 Set $\alpha_{\mathrm{n}} = \alpha_{\mathrm{d}} - \frac{F_{\mathrm{d}}}{F_{\mathrm{d}} - F_{\mathrm{c}}}(\alpha_{\mathrm{d}} - \alpha_{\mathrm{c}})$ and $F_{\mathrm{n}} = F(\boldsymbol{\sigma}_0 + \alpha_{\mathrm{n}}\boldsymbol{C}^{\mathrm{e}}:\Delta\boldsymbol{\varepsilon}^{\mathrm{s}}, K_0)$

2.3.2 If $F_{\mathrm{n}}F_0 > 0$ then set $\alpha_{\mathrm{c}} = \alpha_{\mathrm{n}}$, $F_{\mathrm{d}} = \frac{F_{\mathrm{d}}F_{\mathrm{c}}}{F_{\mathrm{d}} + F_{\mathrm{n}}}$ and $F_{\mathrm{c}} = F_{\mathrm{n}}$.

2.3.3 If $F_{\mathrm{n}}F_0 < 0$ then set $\alpha_{\mathrm{d}} = \alpha_{\mathrm{n}}$ and $F_{\mathrm{d}} = F_{\mathrm{n}}$.

2.4 Set $\alpha = \alpha_{\mathrm{n}}$.

3. Set $\boldsymbol{\sigma}_0 = \boldsymbol{\sigma}_0 + \alpha\boldsymbol{C}^{\mathrm{e}}:\Delta\boldsymbol{\varepsilon}^{\mathrm{s}}$ and $\Delta\boldsymbol{\varepsilon}^{\mathrm{s}} = (1-\alpha)\Delta\boldsymbol{\varepsilon}^{\mathrm{s}}$. Moreover, set $\Delta T = 1$, $T = 0$, $\boldsymbol{\sigma}_{\mathrm{t}} = \boldsymbol{\sigma}_0$ and $K_{\mathrm{t}} = K_0$.

4. Do While $T < 1$,

4.1 Calculate $\Delta\boldsymbol{\sigma}_{\mathrm{a}}$ and $\Delta\boldsymbol{\sigma}_{\mathrm{b}}$ through the following equations:

4.1.1 Evaluate $\Delta\lambda_{\mathrm{t}} = \dfrac{\frac{\partial F}{\partial\boldsymbol{\sigma}_{\mathrm{t}}}:\boldsymbol{C}^{\mathrm{e}}:\Delta\boldsymbol{\varepsilon}^{\mathrm{s}}}{\frac{\partial F}{\partial\boldsymbol{\sigma}_{\mathrm{t}}}:\boldsymbol{C}^{\mathrm{e}}:\frac{\partial g}{\partial\boldsymbol{\sigma}_{\mathrm{t}}} - \frac{\partial F}{\partial K}H_{\mathrm{p}}\sqrt{\frac{2}{3}}\left\|\frac{\partial g}{\partial\boldsymbol{\sigma}_{\mathrm{t}}}\right\|}$ and calculate $\Delta\boldsymbol{\sigma}_{\mathrm{a}} = \Delta T\boldsymbol{C}^{\mathrm{e}}:\Delta\boldsymbol{\varepsilon}^{\mathrm{s}} - \Delta\lambda_{\mathrm{t}}\boldsymbol{C}^{\mathrm{e}}:\frac{\partial g}{\partial\boldsymbol{\sigma}_{\mathrm{t}}}$, $\Delta K_{\mathrm{a}} = \sqrt{\frac{2}{3}}\Delta\lambda_{\mathrm{t}}H_{\mathrm{p}}\left\|\frac{\partial g}{\partial\boldsymbol{\sigma}_{\mathrm{t}}}\right\|$, $\boldsymbol{\sigma}_{\mathrm{a}} = \boldsymbol{\sigma}_{\mathrm{t}} + \Delta\boldsymbol{\sigma}_{\mathrm{a}}$ and $K_{\mathrm{a}} = K_{\mathrm{t}} + \Delta K_{\mathrm{a}}$.

4.1.2 Evaluate $\Delta\lambda_{\mathrm{a}} = \dfrac{\frac{\partial F}{\partial\boldsymbol{\sigma}_{\mathrm{a}}}:\boldsymbol{C}^{\mathrm{e}}:\Delta\boldsymbol{\varepsilon}^{\mathrm{s}}}{\frac{\partial F}{\partial\boldsymbol{\sigma}_{\mathrm{a}}}:\boldsymbol{C}^{\mathrm{e}}:\frac{\partial g}{\partial\boldsymbol{\sigma}_{\mathrm{a}}} - \frac{\partial F}{\partial K}H_{\mathrm{p}}\sqrt{\frac{2}{3}}\left\|\frac{\partial g}{\partial\boldsymbol{\sigma}_{\mathrm{a}}}\right\|}$ and calculate $\Delta\boldsymbol{\sigma}_{\mathrm{b}} = \Delta T\boldsymbol{C}^{\mathrm{e}}:\Delta\boldsymbol{\varepsilon}^{\mathrm{s}} - \Delta\lambda_{\mathrm{a}}\boldsymbol{C}^{\mathrm{e}}:\frac{\partial g}{\partial\boldsymbol{\sigma}_{\mathrm{a}}}$ and $\Delta K_{\mathrm{b}} = \sqrt{\frac{2}{3}}\Delta\lambda_{\mathrm{a}}H_{\mathrm{p}}\left\|\frac{\partial g}{\partial\boldsymbol{\sigma}_{\mathrm{a}}}\right\|$.

4.2 Calculate $\boldsymbol{\sigma}_{\mathrm{b}} = \boldsymbol{\sigma}_{\mathrm{t}} + \frac{\Delta\boldsymbol{\sigma}_{\mathrm{a}} + \Delta\boldsymbol{\sigma}_{\mathrm{b}}}{2}$, $K_{\mathrm{b}} = K_{\mathrm{t}} + \frac{\Delta K_{\mathrm{a}} + \Delta K_{\mathrm{b}}}{2}$ and $R_{\mathrm{n}} = \max\left\{\frac{\|\Delta\boldsymbol{\sigma}_{\mathrm{b}} - \Delta\boldsymbol{\sigma}_{\mathrm{a}}\|}{2\|\boldsymbol{\sigma}_{\mathrm{b}}\|}, \frac{|\Delta K_{\mathrm{b}} - \Delta K_{\mathrm{a}}|}{2|K_{\mathrm{b}}|}, EPS\right\}$.

4.3 If $R_{\mathrm{n}} > STOL$, then $q = \max\left\{0.9\sqrt{\frac{STOL}{R_{\mathrm{n}}}}, 0.1\right\}$, $\Delta T = \max\{q\Delta T, \Delta T_{\min}\}$ and return to item 4.1.

4.4 If $|F(\boldsymbol{\sigma}_{\mathrm{b}}, K_{\mathrm{b}})| > FTOL$, then a drift correction is performed to update $\boldsymbol{\sigma}_{\mathrm{b}}$ and K_{b} as follows:

4.4.1 Set $\boldsymbol{\sigma}_{\mathrm{m}} = \boldsymbol{\sigma}_{\mathrm{b}}$, $K_{\mathrm{m}} = K_{\mathrm{b}}$ and $F_{\mathrm{m}} = F(\boldsymbol{\sigma}_{\mathrm{m}}, K_{\mathrm{m}})$.

4.4.2 Do While $|F_{\mathrm{m}}| > FTOL$

4.4.2.1 Calculate $\delta\lambda = \dfrac{F_{\mathrm{m}}}{\frac{\partial F}{\partial\boldsymbol{\sigma}_{\mathrm{m}}}:\boldsymbol{C}^{\mathrm{e}}:\frac{\partial g}{\partial\boldsymbol{\sigma}_{\mathrm{m}}} - \frac{\partial F}{\partial K_{\mathrm{m}}}H_{\mathrm{p}}\sqrt{\frac{2}{3}}\left\|\frac{\partial g}{\partial\boldsymbol{\sigma}_{\mathrm{m}}}\right\|}$.

4.4.2.2 Calculate $\boldsymbol{\sigma}_{\mathrm{m}} = \boldsymbol{\sigma}_{\mathrm{m}} - \delta\lambda\boldsymbol{C}^{\mathrm{e}}:\frac{\partial g}{\partial\boldsymbol{\sigma}_{\mathrm{m}}}$, $K_{\mathrm{m}} = K_{\mathrm{m}} + \sqrt{\frac{2}{3}}\delta\lambda\left\|\frac{\partial g}{\partial\boldsymbol{\sigma}_{\mathrm{m}}}\right\|$ and $F_{\mathrm{m}} = F(\boldsymbol{\sigma}_{\mathrm{m}}, K_{\mathrm{m}})$.

4.4.2.3 If $|F(\boldsymbol{\sigma}_{\mathrm{m}}, K_{\mathrm{m}})| > |F(\boldsymbol{\sigma}_{\mathrm{b}}, K_{\mathrm{b}})|$, then $\boldsymbol{\sigma}_{\mathrm{m}} = \boldsymbol{\sigma}_{\mathrm{b}} - \dfrac{F(\boldsymbol{\sigma}_{\mathrm{b}}, K_{\mathrm{b}})\frac{\partial F}{\partial\boldsymbol{\sigma}_{\mathrm{b}}}}{\left(\frac{\partial F}{\partial\boldsymbol{\sigma}_{\mathrm{b}}}\right)^T:\frac{\partial F}{\partial\boldsymbol{\sigma}_{\mathrm{b}}}}$ and $K_{\mathrm{m}} = K_{\mathrm{b}}$.

4.4.3 Set $\boldsymbol{\sigma}_{\mathrm{b}} = \boldsymbol{\sigma}_{\mathrm{m}}$ and $K_{\mathrm{b}} = K_{\mathrm{m}}$.

4.5 Set $q = \min\left\{0.9\sqrt{\frac{STOL}{R_{\mathrm{n}}}}, 1.1\right\}$, $\Delta T = \max\{q\Delta T, \Delta T_{\min}\}$ and $\Delta T = \min\{\Delta T, 1 - \mathrm{T}\}$

4.6 Set $T = T + \Delta T$, $\boldsymbol{\sigma}_{\mathrm{t}} = \boldsymbol{\sigma}_{\mathrm{b}}$ and $K_{\mathrm{t}} = K_{\mathrm{b}}$.

5. Set $\boldsymbol{\sigma}_1 = \boldsymbol{\sigma}_{\mathrm{b}}$ and $K_1 = K_{\mathrm{b}}$.

Once the above 5 items are repeated N^{s} times, the stresses and hardening/softening parameter are known at the end of increment which can be used to calculate $\frac{\partial F}{\partial\boldsymbol{\sigma}}$, $\frac{\partial g}{\partial\boldsymbol{\sigma}}$ and $\frac{\partial F}{\partial K}$ at the end of increment. Then, by substituting strain at the end of increment, i.e., $\boldsymbol{\varepsilon} = \boldsymbol{\varepsilon} + \Delta\boldsymbol{\varepsilon}$, into Eq. (10), $\bar{\varepsilon}$ is evaluated and consequently H_{p} is calculated using Eqs. (9) or (10) at the end of increment. Finally, $\boldsymbol{C}^{\mathrm{ep}}$ is evaluated using Eq. (20) that will be used in the construction of the global stiffness equations of the nonlinear finite element analysis.

Typical values for error tolerances in the substepping algorithm described above are: $FTOL = 10^{-9}$, $EPS = 10^{-10}$, $STOL = 10^{-6}$. Moreover, the number of substeps N^{s} is taken to be 10.

4. Material parameters for SFRCs

In this section, the material parameters adopted to check the abilities of the integration algorithm presented in section 3 are specified. Of course, determination of these material parameters requires various sets of experiments where some of them need special facilities. Since the main scope of the present study is to establish an integration algorithm for SFRC and examine it, conducting all these experiments are out of the main scope of the paper. In the following, we first describe two sets of experiments which were used in this study to determine the compressive and split tensile strength of SFRCs as well as to obtain the compressive meridian of SFRCs. We then summarize the material parameters for SFRCs based on these experimental data. Furthermore, material parameters are also given for two other sets of experiments carried out on SFRCs by Chern *et al.* (1993), Pantazopoulou and Zanganeh (2001).

4.1 SFRC specimens

Four different kinds of concrete were investigated. The first one was made without steel fibers and the others were made using the same mixture but adding steel fibers of fraction $V_{\mathrm{f}} = 0.5, 1$ and 2 % (i.e., steel fiber content of 445, 890 and 1780 $\mathrm{N/m^3}$) to the mixture. All mixtures had cement content of 4 $\mathrm{kN/m^3}$ and a cement: water:sand:coarse ratio of 1:0.43:2.73:1.59. Cementitious materials were ordinary Portland cement (ASTM Type II) and silica fume as a pozzolan additive. In order to provide fluidity and workability of the mixture, we used highly effective polycarboxylate chemical additive. The amounts of polycarboxylate used in the mixtures are 0.5% weight of cementitious material. Coarse aggregates used in the concrete mixtures had a nominal maximum size of 9.5 mm and the corrugated steel fibers with a tensile strength > 1100 MPa and $\frac{l_{\mathrm{f}}}{d_{\mathrm{f}}} \equiv 25\mathrm{mm}/0.75\ \mathrm{mm} = 33.3$ were used.

Fig. 2 General view of the 3000-kN capacity testing machine, the rubber bladder and the Hoek cell installed on this machine to apply confining pressure

In order to prepare specimens, we first blended together the cement, silica fume, aggregates and steel fibers in a dry condition. Next, we gradually added water, which was mixed with superplasticizer, to the mixture. We then poured the prepared mixture into cylindrical steel molds and kept these freshly cast specimens in the molds for 24 hours. Finally, we demolded and stored them in water for 28 days. To obtain appropriate results, three replicate specimens were tested and the results were averaged. We prepared 24 cylindrical specimens (150×300 mm) for uniaxial compressive and splitting tensile tests and 60 cylindrical specimens (54×108 mm) for triaxial compressive tests.

4.2 Uniaxial/triaxial compressive tests

Uniaxial compressive tests were conducted on the SFRC specimens with diameter and height of 150×300 mm according to ASTM C39 / C39M – 18. A 3000-kN capacity testing machine, shown in Fig. 2, was used for compression testing, which was conducted under a load control at a rate of 0.25 MPa s^{-1}. This machine was also used for splitting tensile strength testing on similar SFRC specimens in accordance with ASTM C496 and was employed to conduct triaxial compressive tests by installing a Hoek cell as shown in Fig. 2 and explained in the following.

Triaxial compressive tests were performed on the SFRC specimens with diameter and height of 54×108 mm in accordance with ASTM C801. These tests were done under four values of the applied active confining pressure: 5, 10, 15 and 20 MPa. We also utilized a rubber bladder (see Fig. 2) to isolate the specimen from oil penetration. A typical load path for the triaxial compression test with e.g., 15 MPa confining pressure is depicted in Fig. 3. It is illustrated that after applying 5 MPa confining pressure, the axial and confining stresses were simultaneously increased until a specified confining pressure (15 MPa for this case) is attained. While keeping the confining pressure constant, we increase the additional axial stress at a constant stress rate of 0.2 MPa s^{-1} through the platens located at the ends of Hoek cell.

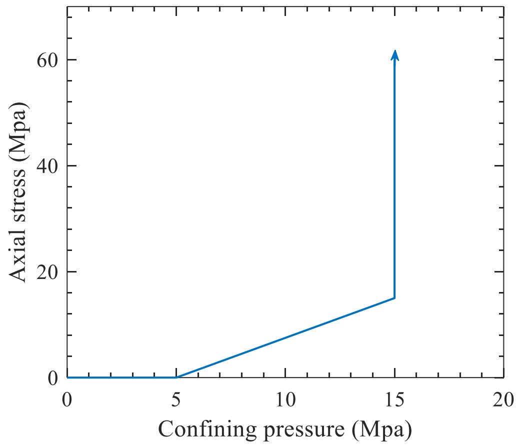

Fig. 3 A typical load path in the triaxial compression test.

4.3 Experimental results for SFRCs and calibrated material parameters

The results of uniaxial compressive and splitting tensile

Table 1 Results of uniaxial and triaxial tests conducted on SFRC specimens

Volume fraction of steel fibers - V_f (%)	Compressive strength (MPa)	Split tensile strength (MPa)	Triaxial peak stresses (MPa) for confining pressures			
			5 MPa	10 MPa	15 MPa	20 MPa
0	33.2	2.89	64.6	83.1	95.2	113
0.5	32.3	3.00	61.3	78.7	90.2	110
1	32.4	3.14	68.5	87.3	99.5	117
2	31.9	3.31	57.6	73.8	89.1	108

tests are summarized in Table 1 for the SFRC specimens. It is evident that the effect of steel fibers on the compressive strength f_c' is mild; however, the tensile strength increases with increasing the volume fraction of steel fibers in agreement with the literature (Balaguru and Shah 1992, Gul *et al*. 2014, Zhang *et al*. 2018). Based on the values for compressive strength of SFRCs given in Table 1, the value of $f_c' = 32$ MPa will be used in our numerical modellings of SFRCs with various contents of steel fiber. The Young's modulus of SFRCs is then estimated via relation $E = 4700\sqrt{f_c'}$ (with f_c' in units of MPa) and given in Table 2.

Table 1 also includes the peak stresses obtained from the triaxial compressive tests conducted on SFRC specimens. The so-called strength enhancement coefficient due to the confining pressure is calculated in the range ~ 3.9 to ~ 6.3 for these SFRCs indicating a high scatter in this coefficient in accordance with the literature (Ansari and Li 1998, Candappa *et al*. 2001, Lan and Guo 1997). The results obtained from the triaxial compressive tests conducted on SFRC specimens are shown in Fig. 4 in terms of mean shear stresses (i.e., τ_{mt} and τ_{mc}) versus mean normal stress (i.e., σ_m) that define compressive meridians for SFRC specimens. It is clear that for the range of stress values considered here the effect of steel fibers on the compressive meridian is mild. Therefore, it is convenient to fit a single curve to all these experimental data to define the compressive meridian. In order to determine the tensile meridian, we have only the experimental results for tensile strength of SFRC specimens. Since we did not carry out true-triaxial tests, the other two points that are required to define the tensile meridian are assumed as follows. The equations of Kupfer *et al*. (1969) were used to determine the biaxial compressive strength (i.e., $\sigma_1 = 0, \sigma_2 = \sigma_3 = 1.16 f_c'$) and the high compressive stress point on the tensile meridian was determined by the Ottosen's failure criteria design charts (Chen 2007) (i.e., $\sigma_1 = 0.06 f_c', \sigma_2 = \sigma_3 = 1.6 f_c'$). These data points are also indicated in Fig. 4. Once the data for compressive and tensile meridians are known, the six parameters in Eq. (4) are calculated as

$$\begin{aligned} a_0 = 0.0827, a_1 = -0.5778, a_2 = -0.1095 \\ b_0 = 0.1162, b_1 = -0.8105, b_2 = -0.1608 \end{aligned} \tag{21}$$

The compressive and tensile meridians that are defined for plain concrete are also plotted in Fig. 4. It should be emphasized that even though this single set of parameters are used in defining the yield surface in the W-W model for SFRCs, two other parameters (i.e., k_t and k_c as given in Eqs. (6)-(7)) are introduced into the meridian functions (see Eqs. (1)-(5)) to account for the effect of the steel fibers. The five parameters of W-W model that are used in the numerical models of SFRCs are thus listed in Table 2.

Table 2 Calibrated material parameters for SFRCs

Parameter	Experiments of the present study	Chern *et al.* (1993) experiments	Pantazopoulou and Zanganeh (2001) experiments
f_c'	32 MPa	20.65 MPa	57.9 MPa
E	26.6 GPa	26 GPa	18.2 GPa
ν	0.2	0.2	0.2
$\hat{a}_0 = \hat{b}_0$	0.099	0.0979	0.2746
$\hat{a}_1$	-0.3709	-1.18	-1.1862
$\hat{a}_2$	-0.9056	-0.6864	-0.2447
$\hat{b}_1$	-0.138	-0.7903	-0.2119
$\hat{b}_2$	-0.5345	-0.2158	-0.4832
A	0.298	0.471	0.193
B	-12.63	-14.61	-15.04

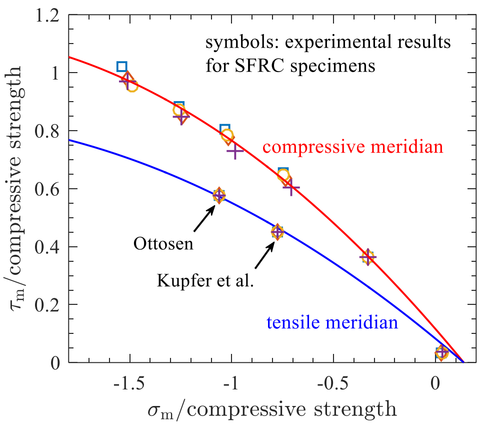

Fig. 4 Peak stresses in the normalized $\tau_m - \sigma_m$ plane. Compressive and tensile meridians for plain concrete with $f_c' = 32$ MPa are also included

It now remains to specify the parameters A and B in the plastic potential function. Since, we did not measure strains in the tests we conducted on SFRC specimens, we estimate the values of strains associated to peak stresses in the uniaxial compressive test and the triaxial compressive test via theoretical stress-strain models proposed for confined concrete (Mander *et al*. 1988). Then, these strains were used to calculate the values of ϕ_1, ϕ_2, $\bar{\rho}_1$ and $\bar{\rho}_2$ as explained in (Grassl *et al*. 2002). Thus, the values of A and B are calculated via relations in Eq. (16) and listed in Table 2.

4.4 SFRCs in the literature and calibrated material parameters

There exists a vast experimental data on the behaviour of SFRCs in the literature (Chern *et al*. 1993, Pantazopoulou and Zanganeh 2001) which can be ideally used in the present study for verification purposes of the numerical results. Table 2 includes material parameters for SFRCs that are obtained from the experiments carried out on SFRCs by Chern *et al*. (1993) as well as by

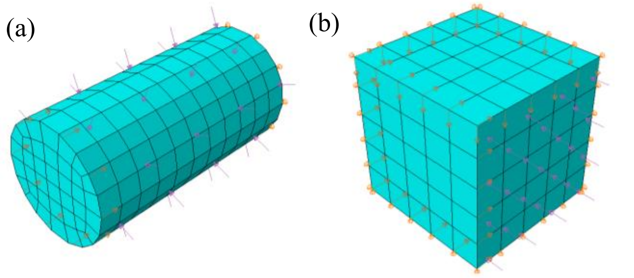

Fig. 5 Finite element mesh and boundary conditions for (a) cylindrical and (b) cubic models of SFRCs

Pantazopoulou and Zanganeh (2001). In order to determine these material parameters, we took a similar approach to that explained above for our experiments. It is worth emphasizing that stress-strain responses for these SFRCs were also reported (Chern *et al*. 1993, Pantazopoulou and Zanganeh 2001) and thus they are employed for validation/verification of our numerical results as presented in section 5.1.

5. Numerical results

The integration scheme explained in section 3 was incorporated into ABAQUS through a UMAT. Two finite element (FE) models were produced: a cylinder and a cube. The FE mesh for these models is shown in Fig. 5 where a C3D8 element, which is an isoparametric, eight-noded solid element, was employed. While the cylindrical model was used for the numerical simulations of SFRCs under uniaxial and triaxial compression loadings, the cubic model was employed for the simulations of SFRCs under true triaxial (e.g., biaxial) loadings. To capture the post-peak (i.e., softening) behavior in the stress-strain responses, a displacement control method was employed to apply the loads in the FEM simulations. This method circumvents the need for adopting arc-length methods in solving FEM nonlinear equations.

We now proceed to present the numerical results using the material parameters given in section 4 in two steps. First, we validate/verify our numerical results by comparing the obtained responses with the experimental data reported in the literature. Then, we present the predicted responses for the SFRCs under various loading conditions to investigate the effects of the confinement stresses as well as the steel fibers. The initial value of the hardening/softening function was taken to be $K_{\text{initial}} = 0.4$ for all the calculations presented in this section.

5.1 Verifications

In order to verify our numerical results, experimental stress-strain data for plain concrete from Kupfer *et al*. (1969) and for SFRCs from Pantazopoulou and Zanganeh (2001), Chern *et al*. (1993) are used.

Numerical results obtained for a plain concrete under uniaxial and biaxial compression are compared in Fig. 6 with the experimental stress-strain data of plain concrete

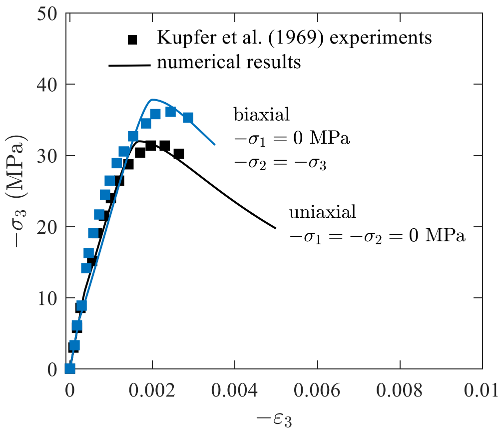

Fig. 6 Stress-strain curves for plain concrete under uniaxial and biaxial loadings.

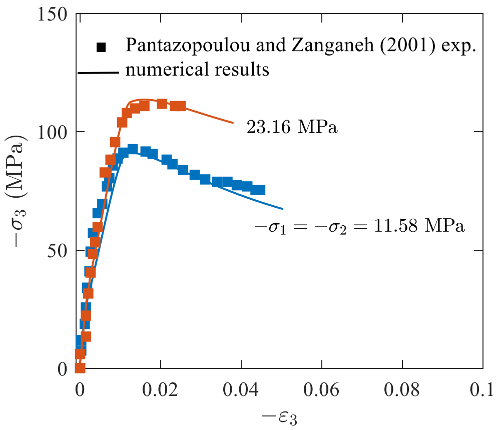

Fig. 7 Laterally confined triaxial stress-strain curves for SFRC with $V_{\text{f}} = (1.2 + 0.8)\%$, $l_{\text{f}}/d_{\text{f}} = 24$ and $f_{\text{c}}' = 57.9$ MPa

reported in Kupfer *et al*. (1969). The plain concrete of Kupfer *et al*. (1969) is very similar to the plain concrete we used in this study, thus the calibrated material parameters given in Table 2 were used for these simulations. Moreover, we specified $\varepsilon_{\text{c}} = 0.00211$ and $\varepsilon_{\text{c}} = 0.00243$ for the uniaxial and biaxial compression simulations, respectively. Fig. 6 shows that the obtained numerical stress-strain curves are in good agreement with the experimental data for plain concrete. It is seen that not only the adopted constitutive model is appropriate for the behavior of plain concrete, as was shown in the literature (Ansari and Li, 1998; Kupfer *et al*. 1969), but also the numerical integration scheme is properly implemented for this constitutive model.

Figs. 7 and 8 show comparisons between the numerical results and the experimental data of SFRCs under triaxial compression reported in Pantazopoulou and Zanganeh (2001), Chern *et al*. (1993). The calibrated material parameters for these simulations were given in Table 2 (see section 4.4). It is also worth emphasizing that the form of equations of parameters a and b that control hardening/softening responses via λ_{f} and f_{c}' (see Eq. (11)) were taken unchanged for these simulations.

The SFRC in Pantazopoulou and Zanganeh (2001) contains $V_{\text{f}} = (1.2 + 0.8)\%$ steel fibers ($l_{\text{f}}/d_{\text{f}} = 24$) and

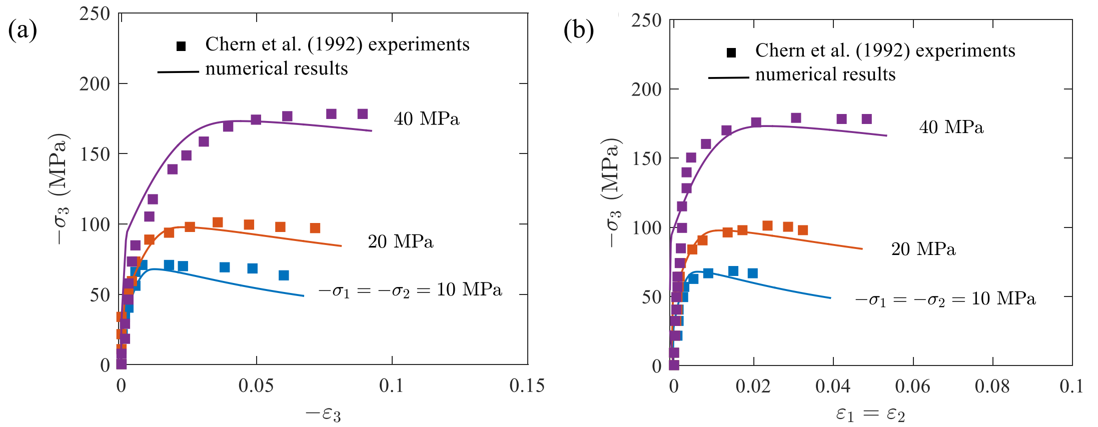

Fig. 8 Laterally confined triaxial stress-strain curves for SFRC with $V_\mathrm{f} = 2\%$, $l_\mathrm{f}/d_\mathrm{f} = 44$ and $f_\mathrm{c}' = 20.65$ MPa: axial stress versus (a) axial strain and versus (b) lateral strains

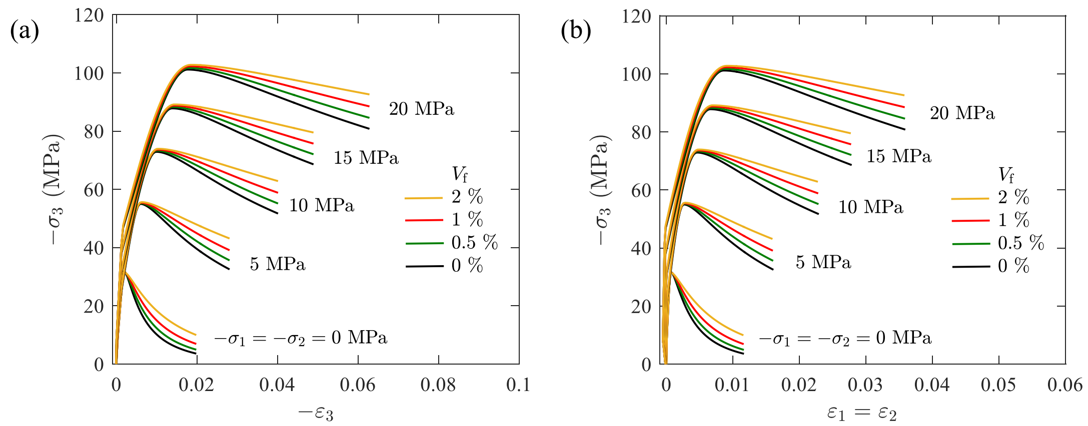

Fig. 9 Laterally confined triaxial stress-strain responses for SFRCs: axial stress versus (a) axial strain and versus (b) lateral strains

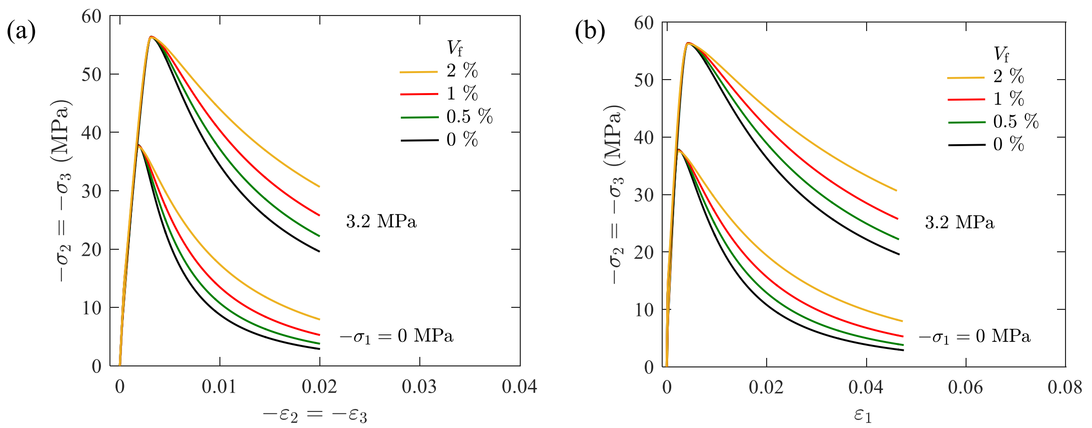

Fig. 10 Predicted stress-strain curves for SFRCs under biaxial and true triaxial loadings: applied stresses versus (a) associated strains and versus (b) lateral strain

has a higher compressive strength compared to SFRCs in our experiments. In addition to the material parameters given in Table 2 that were used for the simulations of these SFRCs, we specified $\varepsilon_\mathrm{c} = 0.0109$ and $\varepsilon_\mathrm{c} = 0.0136$ in the numerical simulations of Fig. 7 for lateral confinement stresses 11.58 MPa and 23.16 MPa, respectively. The numerical stress-strain curves are in very good agreement with the experimental ones. Chern *et al*. (1993) made SFRC specimens with $V_\mathrm{f} = 2\%$ steel fibers ($l_\mathrm{f}/d_\mathrm{f} = 44$) and the compressive strength lower than those we made. In Fig. 8, the stress- strain curves obtained from our numerical simulations on these SFRCs using material parametes given in Table 2 are compared with experimental results. ε_c used in these simulations follows from Eq. (13). The comparisons in Fig. 8 are done in terms of both axial stress versus axial strain curves and axial stress versus lateral

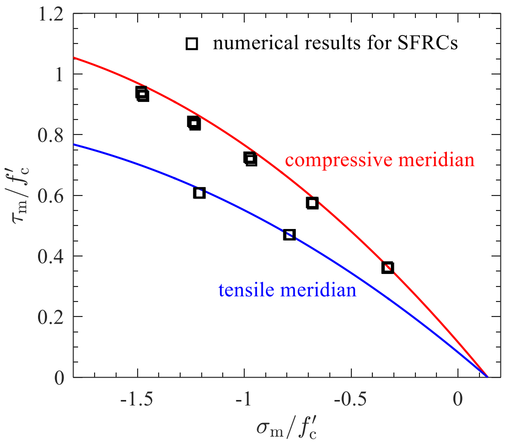

Fig. 11 Predicted peak stresses for the SFRCs under different loading conditions in the normalized $\tau_m - \sigma_m$ plane. Compressive and tensile meridians for plain concrete are plotted for comparison purposes

strain curves. Again, a very good agreement is observed between the numerial results and experimental measurements.

5.2 Predictions

Here, we present predictions of the response of SFRCs with various contents of steel fibers under different loading conditions. Fig. 9 shows numerical results in the form of stress-strain curves for triaxial loading of SFRCs with material parameters given in Table 2. Moreover, biaxial and true-triaxial responses of these SFRCs are plotted in Fig. 10. It is seen from Figs. 9 and 10 that, in line with the literature, the softening response of SFRCs depends strongly on the type of loading, on the confinement stresses and on the steel fiber contents. As it is evident in these figures at a given strain, the larger the volume fraction of fibers, the less the effect of confining pressure on the descending branch of stress-strain curves. This is because the confining pressure holds back the initiation and coalescence of microcracks, resulting in a higher peak deviatoric stress. Although steel fibers have a crack-arrest virtue in fibrous specimens, the presence of confining pressure weakens the capacity of fibers in this respect.

Although we have not compared the numerical results in Figs. 9 and 10 with the experimental stress-strain data, we plot in Fig. 11 the peak stresses obtained from the simulations in the normalized $\tau_m - \sigma_m$ plane. In this figure, the results are compared with the compressive (as obtained from our experiments) and tensile meridians of the SFRCs that were used as input in the numerical analyses. Following the agreement seen in Fig. 11 between the numerical predictions and the model inputs as well as the verifications of the numerical results presented in section 5.1, the stress-strain curves in Figs. 9 and 10 are quite reliable. Therefore, the numerical integration scheme implemented in ABAQUS via UMAT can be used in practical applications when SFRCs need to be modeled via FE analysis.

We close this section by noting that, contrary to the

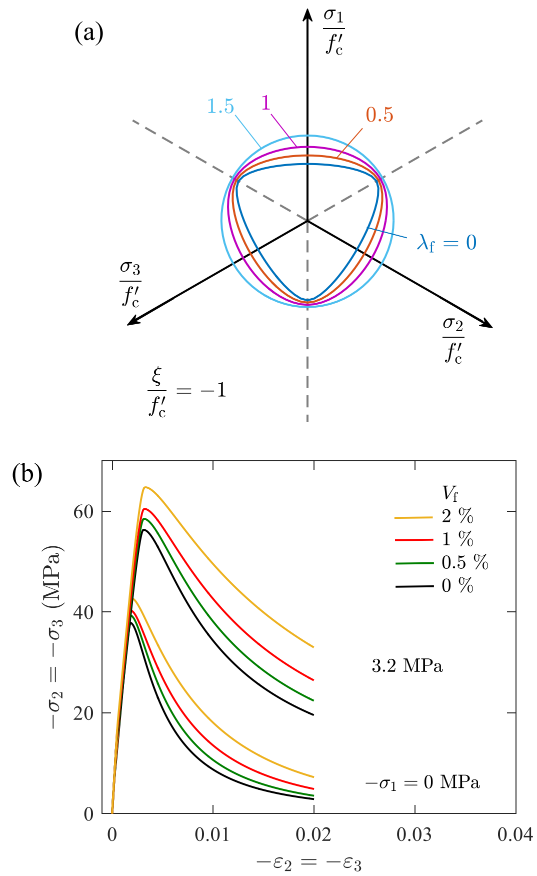

Fig. 12 (a) Variation of yield loci with the change of λ_f in the deviatoric plane when Eq. (22) is employed for k_t in the plasticity model of SFRCs and (b) the associated numerical responses

experiments (e.g., Bao *et al*. 2018), the peak stresses in the stress-strain curves of Fig. 10 only slightly increase with the increase of steel fiber content. This issue is related to the value of k_t calculated from Eq. (6) indicating that this relation cannot capture the effects of steel fibers on the tensile meridian very well and requires a modification based on some new experiments on SFRCs. To further clarify this issue, we repeat simulations presented in Fig. 10 by assuming that

$$k_t = 1 + 0.3\lambda_f\,, \tag{22}$$

while keeping all the other parameters unchanged. Fig. 12a shows the yield loci for SFRC in the deviatoric plane as defined in Eq. (1) for $\xi/f'_c = -1$ and various values of λ_f when Eq. (22) is employed. Specifically, the effect of steel fibers are included in the yield surface via the fiber reinforcement index λ_f through parameters k_t and k_c given in Eqs. (22) and (7), respectively. Fig. 12(b) shows the stress-strain curves obtained from these numerical simulations. It is illustrated in this figure that the peak stresses in the stress-strain curves increase with increasing the steel fiber content. These results are in agreement with experiments (e.g., Bao *et al*. (2018)) and are captured by the use of Eq. (22) instead of Eq. (6). This analysis shows that an experimental investigation is required to accurately define the dependence of k_t on λ_f in SFRCs.

5. Conclusions

The response of SFRCs under multiaxial stresses has been investigated in this study using the finite element analysis that incorporates a plasticity model for the behavior of SFRCs. Following the literature, this model involves the Willam-Warnke failure surface with the relevant hardening/softening functions that control the pre-/post-peak response and a non-associated flow rule for determining the plastic deformations. Experimental data has been employed to determine the various material parameters of the plasticity model of SFRCs. Three sets of parameters have been reported. The first set was from the experiments that we have conducted on SFRC specimens with various contents of steel fibers. The other two sets of parameters were obtained from the experiments that Pantazopoulou and Zanganeh (2001), Chern *et al*. (1993) conducted on SFRCs.

For the integration of the constitutive equations, we have employed the modified explicit substepping algorithm of Sloan *et al*. (2001) which is based on the algorithm of Sloan (1987) with some critical enhancements such as yield intersection and drift correction algorithms. This integration scheme has been implemented in ABAQUS via UMAT. Various numerical simulations have been carried out on SFRCs under multiaxial compression. The numerical results in terms of the stress-strain curves and peak stresses have been found in a very good agreement with the experimental data indicating that not only the adopted plasticity model represents the behavior of SFRCs very well but also the implemented integration scheme can be employed in practical applications of SFRCs.

Predictions of the response of SFRCs with various contents of steel fibers under different loading conditions show that, in line with the literature, the softening response of SFRCs depends strongly on the type of loading, on the confinement stresses and on the steel fiber contents. In laterally confined triaxial stress-strain responses as well as biaxial and true triaxial stress-strain responses predicted by FEM simulations, the larger the volume fraction of fibers, the less the effect of confining pressure on the softening behavior of SFRCs. The effect of steel fibers was included in both the failure surface and the hardening/softening function that controls the evolution of the loading surface via some empirical relations which were determined from the experiments reported in the literature. Our numerical results showed that further research is required to be conducted on SFRCs under multiaxial stresses to accurately determine the relations that incorporate the effects of steel fibers on the failure surface, specifically their effects on the tensile meridian.

References

Amin, A., Foster, S.J., Gilbert, R.I. and Kaufmann, W. (2017), "Material characterisation of macro synthetic fibre reinforced concrete", *Cement Concrete Compos.*, **84**, 124-133. https://doi.org/10.1016/j.cemconcomp.2017.08.018.

Ansari, F. and Li, Q. (1998), "High-strength concrete subjected to triaxial compression", *ACI Mater. J.*, **95**(6), 747-755.

Balaguru, P.N. and Shah, S.P. (1992), *Fiber-Reinforced Cement Composites*, McGraw-Hill. the University of Michigan.

Bao, J., Wang, L., Zhang, Q., Liang, Y., Jiang, P. and Song, Y. (2018), "Combined effects of steel fiber and strain rate on the biaxial compressive behavior of concrete", *Constr. Build. Mater.*, **187**, 394-405. https://doi.org/10.1016/j.conbuildmat.2018.07.203.

Barros, J.A., Gouveia, A.V. and Azevedo, A.F. (2011), "Crack constitutive model for the prediction of punching failure modes of fiber reinforced concrete laminar structures", *Comput. Concrete*, **8**(6), 735-755. https://doi.org/10.12989/cac.2011.8.6.735.

Bažant, Z.P., Caner, F.C., Carol, I., Adley, M.D. and Akers, S.A. (2000), "Microplane model M4 for concrete. I: Formulation with work-conjugate deviatoric stress", *J. Eng. Mech.*, **126**(9), 944-953. https://doi.org/10.1061/(ASCE)0733-9399(2000)126:9(944).

Bitencourt, L.A.G., Manzoli, O.L., Bittencourt, T.N. and Vecchio, F.J. (2019), "Numerical modeling of steel fiber reinforced concrete with a discrete and explicit representation of steel fibers", *Int. J. Solid. Struct.*, **159**, 171-190. https://doi.org/10.1016/j.ijsolstr.2018.09.028.

Blanco, A., Pujadas, P., Cavalaro, S., de la Fuente, A. and Aguado, A. (2014), "Constitutive model for fibre reinforced concrete based on the Barcelona test", *Cement Concrete Compos.*, **53**, 327-340. https://doi.org/10.1016/j.cemconcomp.2014.07.017.

Candappa, D., Sanjayan, J. and Setunge, S. (2001), "Complete triaxial stress-strain curves of high-strength concrete", *J. Mater. Civil Eng.*, **13**(3), 209-215. https://doi.org/10.1061/(ASCE)0899-1561(2001)13:3(209).

Chen, W.F. (2007), *Plasticity in Reinforced Concrete*, J. Ross Publishing.

Chen, W.F. and Han, D.J. (2012), *Plasticity for Structural Engineers*, Springer, New York.

Chern, J.C., Yang, H.J. and Chen, H.W. (1993), "Behavior of steel fiber reinforced concrete in multiaxial loading", *ACI Mater. J.*, **89**(1), 32-40.

Chi, Y., Xu, L. and Yu, H.S. (2013), "Plasticity model for hybrid fiber-reinforced concrete under true triaxial compression", *J. Eng. Mech.*, **140**(2), 393-405. https://doi.org/10.1061/(ASCE)EM.1943-7889.0000659.

Chi, Y., Xu, L. and Yu, H.S. (2014), "Constitutive modeling of steel-polypropylene hybrid fiber reinforced concrete using a non-associated plasticity and its numerical implementation", *Compos. Struct.*, **111**, 497-509. https://doi.org/10.1016/j.compstruct.2014.01.025.

Chi, Y., Xu, L. and Zhang, Y. (2012), "Experimental study on hybrid fiber–reinforced concrete subjected to uniaxial compression", *J. Mater. Civil Eng.*, **26**(2), 211-218. https://doi.org/10.1061/(ASCE)MT.1943-5533.0000764.

Chi, Y., Yu, M., Huang, L. and Xu, L. (2017), "Finite element modeling of steel-polypropylene hybrid fiber reinforced concrete using modified concrete damaged plasticity", *Eng. Struct.*, **148**, 23-35. https://doi.org/10.1016/j.engstruct.2017.06.039.

Chun, B. and Yoo, D.Y. (2019), "Hybrid effect of macro and micro steel fibers on the pullout and tensile behaviors of ultra-high-performance concrete", *Compos. Part B: Eng.*, **162**, 344-360. https://doi.org/10.1016/j.compositesb.2018.11.026.

Dowell, M. and Jarratt, P. (1972), "The "Pegasus" method for computing the root of an equation", *BIT Numer. Math.*, **12**(4), 503-508. https://doi.org/10.1007/bf01932959.

Farnam, Y., Moosavi, M., Shekarchi, M., Babanajad, S.K. and Bagherzadeh, A. (2010), "Behaviour of Slurry Infiltrated Fibre Concrete (SIFCON) under triaxial compression", *Cement Concrete Res.*, **40**(11), 1571-1581.

https://doi.org/10.1016/j.cemconres.2010.06.009.

Grassl, P., Lundgren, K. and Gylltoft, K. (2002), "Concrete in compression: a plasticity theory with a novel hardening law", *Int. J. Solid. Struct.*, **39**(20), 5205-5223. https://doi.org/10.1016/S0020-7683(02)00408-0.

Gul, M., Bashir, A. and Naqash, J. A. (2014), "Study of modulus of elasticity of steel fiber reinforced concrete", *Int. J. Eng. Adv. Technol.*, **3**(4), 304-309.

Guo, Z. (1997), *The Strength and Deformation of Concrete-Experimental Results and Constitutive Relationship*, Tsinghua University Press, Beijing.

Han, J., Zhao, M., Chen, J. and Lan, X. (2019), "Effects of steel fiber length and coarse aggregate maximum size on mechanical properties of steel fiber reinforced concrete", *Constr. Build. Mater.*, **209**, 577-591. https://doi.org/10.1016/j.conbuildmat.2019.03.086.

Hibbit, D., Karlsson, B. and Sorenson, P. (2005), *ABAQUS Reference Manual 6.7*, ABAQUS Inc. Pawtucket.

Imran, I. and Pantazopoulou, S. J. (2001), "Plasticity model for concrete under triaxial compression", *J. Eng. Mech.*, **127**(3), 281-290. https://doi.org/10.1061/(ASCE)0733-9399(2001)127:3(281).

Jiang, J.F., Xiao, P.C. and Li, B.B. (2017), "True-triaxial compressive behaviour of concrete under passive confinement", *Constr. Build. Mater.*, **156**, 584-598. https://doi.org/10.1016/j.conbuildmat.2017.08.143.

Kupfer, H., Hilsdorf, H.K. and Rusch, H. (1969), "Behavior of concrete under biaxial stresses", *ACI J. Proc.*, **66**(8), 656-666.

Lan, S. and Guo, Z. (1997), "Experimental investigation of multiaxial compressive strength of concrete under different stress paths", *ACI Mater. J.*, **94**(5), 427-434.

Lee, S., Park, Y. and Abolmaali, A. (2019), "Investigation of flexural toughness for steel-and-synthetic-fiber-reinforced concrete pipes", *Struct.*, **19**, 203-211. https://doi.org/10.1016/j.istruc.2018.12.010.

Liang, X. and Wu, C. (2018), "Meso-scale modelling of steel fibre reinforced concrete with high strength", *Constr. Build. Mater.*, **165**, 187-198. https://doi.org/10.1016/j.conbuildmat.2018.01.028.

Lu, X. and Hsu, C.T.T. (2006), "Behavior of high strength concrete with and without steel fiber reinforcement in triaxial compression", *Cement Concrete Res.*, **36**(9), 1679-1685. https://doi.org/10.1016/j.cemconres.2006.05.021.

Mander, J.B., Priestley, M.J. and Park, R. (1988), "Theoretical stress-strain model for confined concrete", *J. Struct. Eng.*, **114**(8), 1804-1826. https://doi.org/10.1061/(ASCE)0733-9445(1988)114:8(1804).

Othman, H. and Marzouk, H. (2018), "Applicability of damage plasticity constitutive model for ultra-high performance fibre-reinforced concrete under impact loads", *Int. J. Impact Eng.*, **114**, 20-31. https://doi.org/10.1016/j.ijimpeng.2017.12.013.

Pantazopoulou, S.J. and Zanganeh, M. (2001), "Triaxial tests of fiber-reinforced concrete", *J. Mater. Civil Eng.*, **13**(5), 340-348. https://doi.org/10.1061/(ASCE)0899-1561(2001)13:5(340).

Perumal, R. (2014), "Performance and modeling of high-performance steel fiber reinforced concrete under impact loads", *Comput. Concrete*, **13**(2), 255-270. https://doi.org/10.12989/cac.2014.13.2.255.

Poorhoseina, R. and Nematzadeh, M. (2018), "Mechanical behavior of hybrid steel-PVA fibers reinforced reactive powder concrete", *Comput. Concrete*, **21**(2), 167-179. https://doi.org/10.12989/cac.2018.21.2.167.

Ren, Y., Yu, Z., Huang, Q. and Ren, Z. (2018), "Constitutive model and failure criterions for lightweight aggregate concrete: A true triaxial experimental test", *Constr. Build. Mater.*, **171**, 759-769. https://doi.org/10.1016/j.conbuildmat.2018.03.219.

Rodrigues, E.A., Manzoli, O.L., Bitencourt, L.A.G., Bittencourt, T.N. and Sánchez, M. (2018), "An adaptive concurrent multiscale model for concrete based on coupling finite elements", *Comput. Meth. Appl. Mech. Eng.*, **328**, 26-46. https://doi.org/10.1016/j.cma.2017.08.048.

Sloan, S.W. (1987), "Substepping schemes for the numerical integration of elastoplastic stress–strain relations", **24**(5), 893-911. https://doi.org/10.1002/nme.1620240505.

Sloan, S.W., Abbo, A.J. and Sheng, D. (2001), "Refined explicit integration of elastoplastic models with automatic error control", *Eng. Comput.*, **18**(1/2), 121-194. https://doi.org/10.1108/02644400110365842.

Smolčić, Ž. and Ožbolt, J. (2017), "Meso scale model for fiber-reinforced-concrete: Microplane based approach", *Comput. Concrete*, **17**(4), 375-385. https://doi.org/10.12989/cac.2017.19.4.375.

Swaddiwudhipong, S. and Seow, P.E.C. (2006), "Modelling of steel fiber-reinforced concrete under multi-axial loads", *Cement Concrete Res.*, **36**(7), 1354-1361. https://doi.org/10.1016/j.cemconres.2006.03.008.

William, K.J. and Warnke, E.P. (1975), "Constitutive model for the triaxial behavior of concrete", *Int. Assoc. Bridge Struct. Eng. Pr.*, **19**, 1-30.

Zhang, Y., Zhao, K., Li, Y., Gu, J., Ye, Z. and Ma, J. (2018), "Study on the local damage of SFRC with different fraction under contact blast loading", *Comput. Concrete*, **22**(1), 63-70. https://doi.org/10.12989/cac.2018.22.1.063.

CC